

Application of Non-Precious Bifunctional Catalysts for Metal-Air Batteries

Steffen Haller,* Vladislav Gridin, Kathrin Hofmann, Robert W. Stark, Barbara Albert, and Ulrike I. Kramm*

Zinc-air batteries have several advantages in comparison with the lithium-ion technology as they enable the use of earth-abundant elements, work at low cost, are lightweight, and are also much safer in application. In addition to the chemistry related to the zinc electrode, efficient and stable bifunctional catalysts are required for oxygen reduction reaction (ORR, for discharging) and oxygen evolution reaction (OER, for charging) on the air-electrode side. Herein, a family of non-precious metal catalysts is investigated as possible bifunctional composite: metal–nitrogen–carbon (MNC) catalysts for ORR, and metal oxyhydroxides as OER catalysts (Ox). The effect of transition metal and metal loading in these composite MNC + Ox catalysts on ORR and OER activities in half-cell measurements is discussed. The catalysts were characterized using X-ray diffraction and Raman spectroscopy to identify their phase composition. For the most active material, a potential gap of 0.79 V between OER and ORR was obtained, respectively. In a zinc-air cell, this catalyst moreover showed a peak power density of 62 mW cm^{-2} and a charge–discharge gap of 0.94 V after 26 h of charge–discharge cycling.

Among these devices, zinc-air batteries consisting of an air-breathing cathode and a zinc anode stand out for their high theoretical energy density as well as their low-cost fabrication and operation.^[1b,3] Despite these advantages, the widespread application of zinc-air batteries has been hampered by several problems associated with metal anodes, bifunctional air catalysts, and electrolytes.^[4] One of the main challenges remains the development of a highly active and durable bifunctional oxygen electrocatalyst for air cathodes.^[5] Such catalysts have to catalyze both the oxygen reduction reaction (ORR, during discharging) and the oxygen evolution reaction (OER, during charging) but they also have to stay stable under both reaction conditions. To reduce the use of expensive state-of-the-art noble metals, various materials like perovskites,^[6] transition metal oxides,^[7] sulfides,^[8] nitrides,^[9] and carbonaceous materials^[10] have been investi-

1. Introduction

To face the challenges of the climate change and the rapidly growing world population, efficient and environmentally friendly energy storages are needed to provide power for electric devices, vehicles, and grid-scale energy sources.^[1] In the past years, metal-air batteries have gained revived interest to offer an alternative to the almost impossible to improve lithium-ion technology.^[2]


gated as noble metal-free catalysts. Among carbonaceous materials, heteroatom-doped carbon has drawn a lot of interest because of its high electrical conductivity, high surface area, and good stability.^[11]

Transition metal-containing nitrogen-doped carbon (MNC) catalysts, especially of the FeNC type, have been reported to show excellent ORR activity in both acidic and alkaline conditions.^[12] Typically, the preparation of FeNC involves an acid leaching step to remove side phases,^[13] as the ORR is attributed to FeN₄-centers (or MN₄).^[14] Side phases can be, e.g., oxides, nitrides or carbides,^[15] hence species which are of interest for Me-air batteries. Varying the incorporation of transition metals in N-doped carbon structures has shown to be a promising approach for synthesizing bifunctional catalysts.^[16]

The aim of this work is to contribute to the development of efficient and durable bifunctional MNC catalysts for zinc-air batteries. To find the optimum in terms of overpotentials, polypyrrole nanotubes are doped with various transition metals via a simple impregnation method followed by microwave pyrolysis, and the influence of the metal on the bifunctional OER/ORR activity is investigated. This is followed by the optimization of Co loading that turned out best in performance and was thus tested in a single cell. It is shown that the simple preparation leads to promising bifunctional catalysts that exhibit excellent cycling stability.

S. Haller, V. Gridin, Dr. K. Hofmann, Prof. B. Albert, Prof. U. I. Kramm
Eduard-Zintl-Institute for Physical and Inorganic Chemistry
TU Darmstadt
64287 Darmstadt, Germany
E-mail: steffen.haller@tu-darmstadt.de; ulrike.kramm@tu-darmstadt.de

Prof. R. W. Stark
Physics of Surfaces
TU Darmstadt
64287 Darmstadt, Germany

 The ORCID identification number(s) for the author(s) of this article can be found under <https://doi.org/10.1002/ente.202001106>.

© 2021 The Authors. Energy Technology published by Wiley-VCH GmbH. This is an open access article under the terms of the Creative Commons Attribution-NonCommercial License, which permits use, distribution and reproduction in any medium, provided the original work is properly cited and is not used for commercial purposes.

DOI: 10.1002/ente.202001106

2. Results and Discussion

Two variation series were explored related to their capabilities of application in Zn-air batteries. At first, the variation of metal species should be discussed.

Figure 1a shows the X-ray diffractograms of the catalysts prepared with different transition metals. For Fe- and Mo-based samples, no obvious reflections could be tracked by X-ray diffraction (XRD), they appear X-ray amorphous under the given conditions. For all other samples the reflections can be assigned to one single crystalline phase. For Co0.20/PPy, the reflections are located at 2θ values of 44.0° , 51.3° , and 75.3° and can be assigned to α -cobalt.^[17] The diffractograms of V0.20/PPy and W0.20/PPy, respectively, shows the characteristic reflection pattern of vanadium nitride (VN)^[18] and tungsten carbide (WC).^[19] This assignment is supported by the identified bands in the Raman spectra of the samples in **Figure 1b**. In case of Co0.20/PPy, Fe0.20/PPy, and V0.20/PPy, oxidic species can be identified. For Co0.20/PPy bands at 465 , 515 , and 655 cm^{-1} can be assigned to spinel-type Co_3O_4 .^[20] The bands at 220 , 280 , 387 , and 595 cm^{-1} as identified in Fe0.20/PPy can be related to Fe_3O_4 .^[21] In the spectrum of V0.20/PPy, the band at 820 cm^{-1} can be assigned to VO_2 and the bands at 884 and 918 cm^{-1} are assigned to mixed vanadium oxides, VO_x .^[22] It is assumed that a laser-induced oxidation might have led to the formation of oxidized surfaces of metallic particles as these oxides were not identified by XRD. Indeed, a similar process is described in the literature for a pulsed laser-induced oxidation of iron samples.^[23] All samples exhibit a pronounced presence of G and D bands of carbon associated to graphitic and defect-rich graphene, respectively.^[24] The I_G/I_D ratio might

thus be used as a measure of graphitization. All catalysts give similar ratios of 0.5, except for V0.20/PPy, where the value is close to 1.0. It remains unclear, if this observation is indeed indicative of a stronger degree of graphitization, as a strong baseline distortion from the intense VN bands in the spectrum might have hindered an accurate background subtraction. In case of Mo- and W-based catalysts, a shoulder appears at 1660 cm^{-1} that might be related to oxidized carbon.^[25] It is known for transition metals, e.g., Co, Fe, Ni, that they can act as graphitization catalyst during oven pyrolysis.^[26] Based on this, a similar behavior might be assumed for such metals during microwave heating. However, the Fe- and Co-based catalysts do not provide any evidence of stronger graphitization compared to the other metals. As stated earlier, it is the vanadium-based catalyst that seem to have the largest graphene layer extension. A possible origin of this might be found in the different heating mechanism in a microwave compared with conventional pyrolysis, which results in fast heating of polarizable materials like carbon supports.^[27] Under microwave irradiation, metals can cause structural conversions of the surrounding carbon material, while this might be overlaid by a heat transfer from supporting carbon.^[28] In general, the effect of the metal on the graphitization of carbon in a microwave is still not fully understood but goes beyond the scope of this article.^[29]

Prior to testing OER and ORR activities, the cyclic voltammograms (CVs) of the catalysts were recorded in N_2 -saturated electrolyte (**Figure 2a**). The corresponding CVs in O_2 -saturated electrolyte are shown in **Figure S1**, Supporting Information. The added metals strongly influence the obtained behavior. For Co0.20/PPy, an increase in current density is observed in the anodic sweep above 0.9 V . This might be attributed to the transition from Co(II) to Co(III), corresponding to the oxidation from either Co_3O_4 , CoO, or passivated cobalt ($\text{Co}(\text{OH})_2$) to CoOOH .^[30] The catalysts were then subjected to testing of OER activity and ORR activity. For the OER activity (**Figure 2b**), Co0.20/PPy exhibited the lowest onset potential of 1.54 V and the lowest Tafel slope of 70 mV dec^{-1} (**Figure S2a**, Supporting Information). The OER activity of cobalt oxides has been investigated by various researchers.^[30a,30b,31] They uniformly suggested that during anodic polarization of cobalt oxides, Co(IV) species are formed which mediate the initial OER step of OH^- ion adsorption. This Co0.20/PPy shows similar performance compared with other Co-oxide based catalysts, when the required overpotential to reach 10 mA cm^{-2} is considered.^[32] The OER activity of all other catalysts is much lower with at least 50 mV higher onset potentials. The overall observed activities follow the order: $\text{Co0.20/PPy} > \text{W0.20/PPy} > \text{PPy} > \text{V0.20/PPy} > \text{Fe0.20/PPy} \approx \text{PPy-uw} > \text{Mo0.20/PPy}$.

The trend during rotating disc electrode (RDE) experiments to obtain the ORR activity changes slightly, as shown in **Figure 2c**. It is worth noticing that the pyrolyzed PPy and PPy-uw already show high intrinsic ORR activity with an onset potential of 0.91 V even without addition of a transition metal after the polymerization step but prior to microwave heating. This might be explained as following: as the oxidative polymerization of pyrrole is initiated by iron(III) chloride specifically the unwashed PPy-NT will contain iron residuals from the polymerization step. But even after several washing steps, iron might be present to some extent in the washed PPy-NT. Based on the fact, that the ORR performance data of these two reference samples are

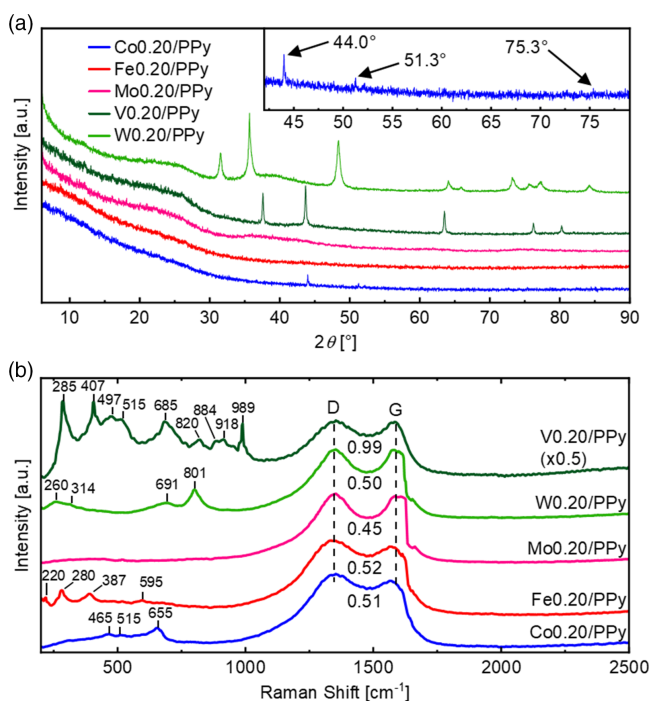


Figure 1. Transition metal variation series: a) X-ray diffractograms with enlarged section of the diffractogram of Co0.20/PPy, b) Raman spectra with I_G/I_D ratios and bands assigned to various metal containing species as discussed in the main text.

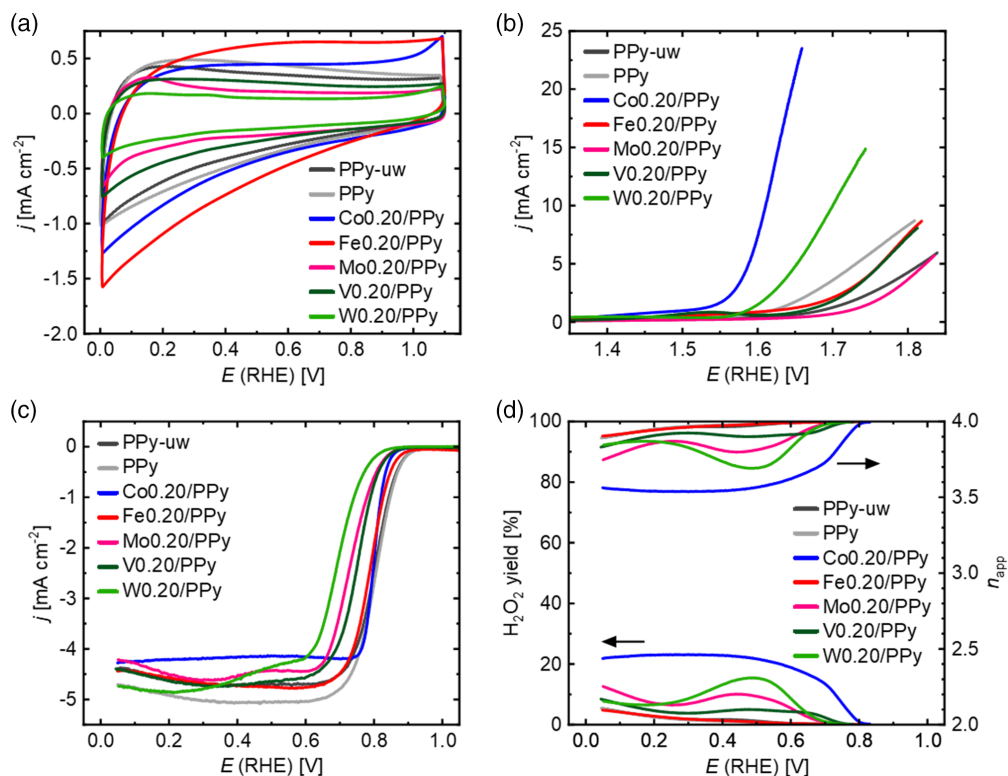


Figure 2. Transition metal variation series: a) CVs in N₂-saturated 0.1 M KOH, b) OER curves in N₂-saturated 0.1 M KOH, c) RDE curves in O₂-saturated 0.1 M KOH at 1500 rpm, and d) peroxide yields and apparent electron transfer numbers determined from ring and disc currents during ORR.

comparable with Fe0.20/PPy, we assume that indeed such iron residuals cause the formation of ORR-active FeN₄ sites during microwave pyrolysis. Similarly, iron-based oxides might contribute to the OER activity. The variation in activities of Fe0.20/PPy, PPy-w, and PPy-uw might be attributed to changing contributions of FeN₄ versus oxidized species as function of the variation of iron content in these samples. This assumption is further supported by the trends observed for the cobalt variation series discussed in the second part of this article (see in the following sections). Nonetheless, the type of added transition metal still influences the ORR performance. Co0.20/PPy shows a slightly later onset potential of 0.87 V compared with Fe0.20/PPy (0.90 V). Considering half-wave potentials, the activity decreases in the order: PPy > PPy-uw \approx Fe0.20/PPy > Co0.20/PPy > V0.20/PPy > Mo0.20/PPy > W0.20/PPy. The Tafel slopes (Figure S2b, Supporting Information) are in the expected range typically observed for MNC catalysts^[33] while it is much lower for Co0.20/PPy.

Figure 2d shows the relative hydrogen peroxide yield as well as the corresponding electron transfer numbers n_{app} . The ratio of formed peroxide and the corresponding apparent electron transfer number n_{app} was determined from disc and ring currents during rotating ring-disc electrode (RRDE) measurements. In the range between 0.6 and 0.2 V, Fe0.20/PPy provides the lowest amount of formed hydrogen peroxide, that was also expected based on the already excellent selectivity of these catalysts in acidic electrolyte.^[34]

Co0.20/PPy shows the highest peroxide formation with $\approx 20\%$, which corresponds to an electron transfer number of

3.5–3.6. The relatively high peroxide yield might be caused by a dual-site ORR mechanism, which was proposed by Olson et al.^[35] for cobalt-based catalysts in alkaline conditions. In addition, determination from ring and disc current (n_{app}), the electron transfer numbers n_{KL} can be determined by Koutecký–Levich (KL) analysis. The corresponding RDE data and KL plots can be found in Figure S3 and S4, Supporting Information. While in principle n_{KL} and n_{app} should give similar values, often RRDE experiments overestimate the direct reduction of oxygen to water.^[36] To compare both values, Figure 3a shows both values n_{app} and n_{KL} . For Co0.20/PPy, the data point is closest to $n_{KL}/n_{app} = 1$. All other samples exhibit higher n_{app} values compared with n_{KL} . This might be explained by diffusion limitation of the formed peroxide intermediates. Depending on the porosity of the catalyst, the peroxide might be trapped in the pores and readsorb on an additional active site followed by a second two-electron reduction step.

For metal-air application, a catalyst should ideally combine small overpotentials for both reactions, ORR and OER. Therefore, in Figure 3b, the different catalysts are compared with respect to the potentials at half-wave potential $E_{1/2}$ (ORR) and at OER current densities of 5 and 10 mA cm⁻². While the last named current density equals the state-of-the-art for benchmarking of OER catalysts,^[37] it is unfortunately not reached by all catalysts. Based on this, the metal variation series is specifically compared for the difference in half-wave potential $E_{1/2}$ (ORR) and $E_{5 \text{ mA cm}^{-2}}$ (OER). ΔE increases in the order: Co0.20/PPy \ll PPy < W0.20/PPy < Fe0.20/PPy < PPy-uw \approx V0.20/PPy < Mo0.20/PPy. Thus, the comparison clearly shows that the use of cobalt out of the group of investigated metals seems most

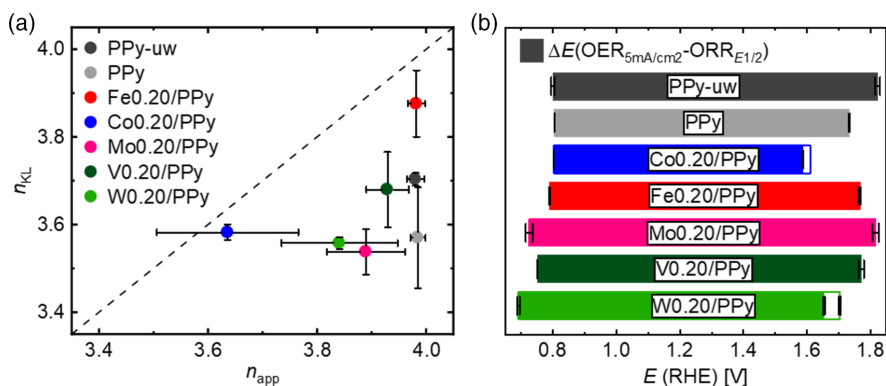


Figure 3. a) Correlation between n_{app} and n_{KL} . The dashed line indicates a slope of 1. b) Comparison of the bifunctional activities of the transition metal variation catalysts between $E_{1/2}$ (ORR) and $E_{5 mA cm^{-2}}$ (OER). For Co0.20/PPy and W0.20/PPy, the nonhatched segments also indicate $E_{10 mA/cm^2}$ (OER) that is the common benchmarking potential but that was not reached for the other catalysts in the investigated potential range.

promising for bifunctional use. Therefore, it was further explored, if the performance can be further optimized by variation of the cobalt loading.

To investigate the influence of cobalt loading on the catalytic activity, different mole equivalents (0.05, 0.10, 0.24, and 0.40 mmol) were used in the preparation. Figure 4 shows the diffraction patterns and the Raman spectra of the cobalt content variation series.

The sharp XRD reflections of Co0.20/PPy, Co0.24/PPy, and Co0.40/PPy indicate the presence of highly crystalline cobalt particles, and the intensities increase with increasing Co loading in the precursor. For Co0.05/PPy and Co0.10/PPy, it is suggested that these samples contain cobalt loadings below the detection

limit of the diffractometer and thus α -cobalt peaks are not observed in their diffractograms. Moreover, the cobalt oxide-related Raman bands get more pronounced, specifically at $660 cm^{-1}$. Such behavior was expected, as with increasing cobalt loading, at constant amount of nitrogen, above a certain limit a proper formation of CoN_4 sites should not be possible. Similar observations were made before for cobalt- or iron-based MNC catalysts.^[14a,38] Instead, it is expected that the increasing size of crystalline cobalt domains leads to higher amounts of OER active^[39] cobalt oxides and/or hydroxides, when exposed to air as well as under OER conditions. In addition to crystalline cobalt, additional phases might form, like Co-rich nitride-like Co_xN_y species, which might also undergo surface oxidation when exposed to air.

Unfortunately, it is impossible to infer to which degree the sample with lowest cobalt content contains additional cobalt phases in addition to CoN_4 . Such small amounts or domains would be below the detection limit of XRD and Raman spectroscopy. Thus, for further verification, additional spectroscopic analysis or high-resolution imaging will be required in the future. Nevertheless, it should be pointed out that the other phases might be relevant contributors especially to the OER activity.

In the following, the impact of cobalt loading on the electrocatalytic activities for the ORR and OER will be discussed. Figure 5 shows the comparison of the CVs, the RDE curves at 1500 rpm, the OER linear sweep voltammograms, and the hydrogen peroxide formation and apparent number of transferred electrons. The CVs in O_2 -saturated versus N_2 -saturated electrolyte are shown in Figure S5, Supporting Information.

With increasing cobalt content, the current density above 0.9 V and associated with the anodic Co(II) to Co(III) transition becomes more intense. For Co0.40/PPy, two cathodic peaks at 1.07 and 0.92 V might be assigned to the stepwise reduction of dispersed Co(III) to Co(II) oxide layers.^[30b]

The ORR performance does not significantly change with increasing cobalt loading (Figure 5b). The catalysts show very similar onset potentials of about 0.80–0.81 V, as well as almost identical Tafel slopes (Figure S6b, Supporting Information) and half-wave potentials. This would be in agreement with the assumption that CoN_4 sites might be the main contributors to

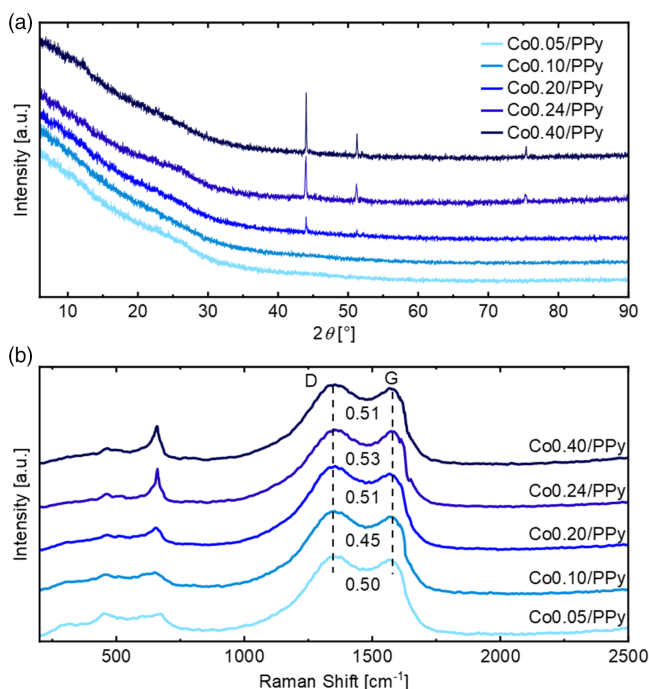


Figure 4. Characterization of the catalysts prepared with different cobalt loadings: a) X-ray diffractograms and b) Raman spectra with I_G/I_D ratios.

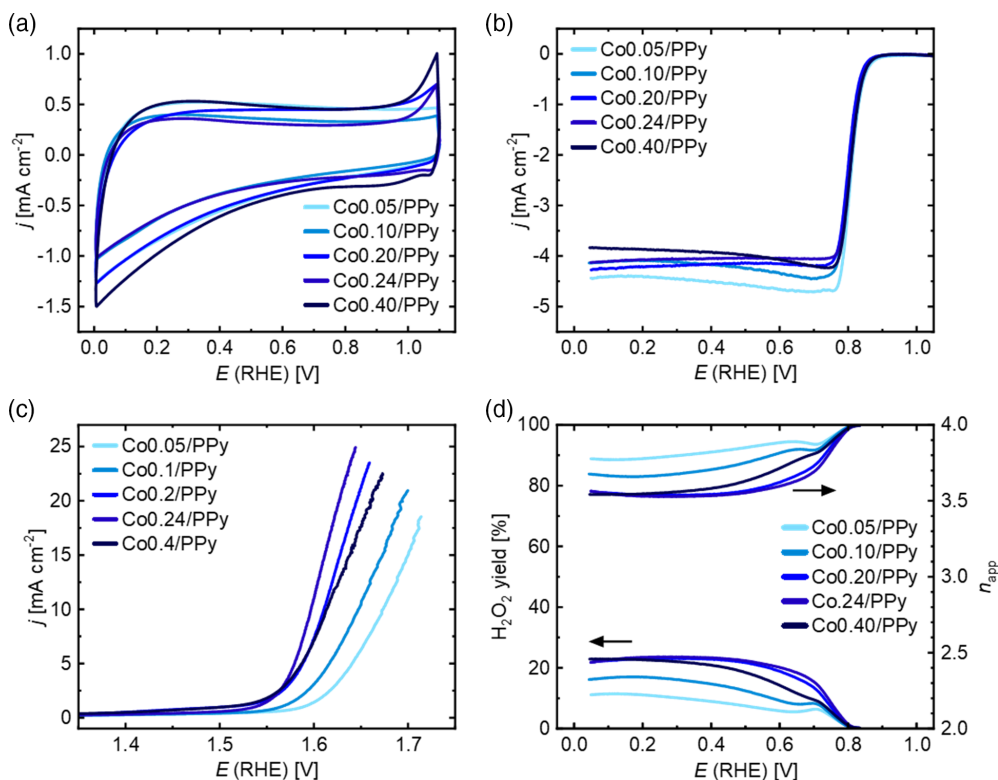


Figure 5. Cobalt loading variation series: a) CVs in N_2 -saturated electrolyte, b) ORR curves in O_2 -saturated electrolyte at 1500 rpm, c) OER curves in N_2 -saturated electrolyte, d) peroxide yields and apparent electron transfer numbers during ORR.

the ORR activity. A major difference can however be found in the diffusion limiting current density and hydrogen peroxide formation. The peroxide formation increases from $\approx 10\%$ to 20% for Co0.20/PPy and Co0.24/PPy. Also Co0.40/PPy remains on a high level, but gives slightly less values.

As shown in Figure 5c, the OER improves, indicated by a decrease in the onset potential from 1.60 V for Co0.05/PPy to 1.53 V obtained for Co0.24/PPy. The sample with highest cobalt content, however, performs again worse. This is also reflected by the Tafel slopes which is lowest for Co0.24/PPy (52 mV dec^{-1} , Figure S6a, Supporting Information) and indicates that there is an optimal cobalt amount for OER catalysis equal to 0.24 mole equivalents in this work.

We would like to highlight that the most active OER catalyst is the same that leads to the highest peroxide yield.

In contrast to n_{app} (from RRDE), the values n_{KL} (from Koutecký–Levich plots, see Figure S7, Supporting Information, for the related RDE curves and Figure S8, Supporting Information, for the KL plots) suggest that the four-electron path is more likely for higher cobalt loadings (Figure 6a). Remarkably, the determined n_{app} values of the two catalysts with highest cobalt loadings, Co0.24/PPy and Co0.40/PPy are higher than n_{KL} . Here, a varying degree of different cobalt species could be at the origin of the differing selectivity trends. The observed trends and assignment to different cobalt environments for ORR activity and selectivity as well as OER activity are further supported from the comparison of an as-prepared Co0.24/PPy and after acid leaching. It is known that metallic and oxidic species will be drastically lowered in their content by such a

treatment, whereas MN_4 centers will remain intact.^[40] In line with our interpretation, the OER activity as well as the peroxide yields are significantly lowered, while no change in ORR kinetics is observed. The related electrochemical data can be found in Figure S9, Supporting Information. This leads to the suggestion that the additional inorganic phases contribute to OER as well as to peroxide formation, whereas the ORR activity is more related to acid-resistant sites within the carbonaceous structure like FeN_4 (with Fe residuals from oxidative polymerisation of pyrrole) or CoN_4 sites.

The obtained parameters of OER and ORR activity of the most active catalyst obtained in this work is shown in Table 1 and compared with literature data. It has a potential difference of only 0.79 V for achieving an OER current of 10 mA cm^{-2} and the $E_{1/2}$ value related to ORR. This compares well with other bifunctional nonprecious metal MNC catalysts reported in literature.

In order to study the effect of cobalt loading on real device applications, Co0.10/PPy and Co0.24/PPy were tested for their activity and stability in a zinc-air battery.

Figure 7a shows a picture of the cell. The measured open-circuit voltages (OCVs) of the cells were 1.420 V for Co0.10/PPy and 1.433 V for Co0.24/PPy in comparison with a theoretical value of 1.6 V. Both catalysts exhibited nearly identical performance prior to cycling, with a peak power density of 61.5 mW cm^{-2} at 99.5 mA cm^{-2} for Co0.10/PPy and 62.4 mW cm^{-2} at 102.5 mA cm^{-2} for Co0.24/PPy (Figure 7b, curves i). As the polarization curve displays the behavior during discharging,

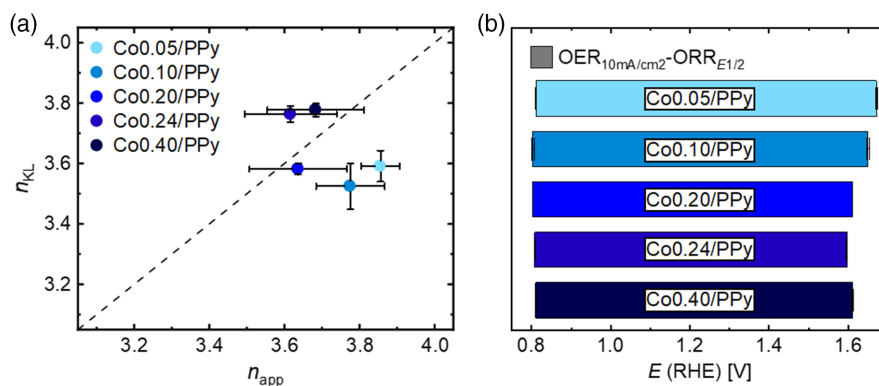


Figure 6. a) Correlation between n_{app} and n_{KL} and b) comparison of the bifunctional activities of the cobalt loading variation catalysts.

Table 1. OER and ORR activities of various bifunctional catalysts.

Sample	Description	Electrolyte	Loading [$mg\ cm^{-2}$]	$E_{10mA\ cm^{-2}}$ [V]	$E_{1/2}$ [V]	$\Delta E_{OER-ORR}$ [V] ^{a)}	Reference
Co0.24/PPy	Co-impregnated PPy-NTs	0.1 M KOH	0.5	1.60	0.81	0.79	This work
C-MOF-C2-900	Co in MOF-derived N-doped carbon	0.1 M KOH	0.2	1.58	0.82	0.76	[42]
MSZIF-900	Co supported on N-doped CNTs	1 M KOH (OER) 0.1 M KOH (ORR)	0.286	1.57	0.84	0.73	[43]
FeNx-PNC	Fe in porous N-doped carbon	0.1 M KOH	0.14	1.63	0.86	0.77	[44]
NGM-Co	Co-N _x -C species in graphene	0.1 M KOH	0.25	1.73	0.78	0.95	[45]
Co-N _x /C NRA	Co-N _x /C nanorod arrays	0.1 M KOH	0.5	1.53	0.88	0.65	[46]
FeCo-N-C-700	Fe, Co in MOF-derived N-doped carbon	0.1 M KOH	0.4	1.61	0.90	0.71	[47]
NCAG/Fe-Co	Fe, Co dispersed in carbon aerogel	1 M KOH (OER) 0.1 M KOH (ORR)	0.425	1.53	0.89	0.64	[48]
N-GCNT/FeCo-3	FeCo alloy in N-doped carbon nanotubes	0.1 M KOH	0.2	1.73	0.92	0.81	[49]
N-carbon	Metal-free defective nanocarbon	0.1 M KOH	0.146	1.65	0.74	0.91	[50]

^{a)}At $E_{OER} = 10\ mA\ cm^{-2}$, $E_{ORR} = E_{1/2}$.

i.e., during ORR, the similar performance of the catalysts might be attributed to their nearly identical ORR performance.

When the stability behavior during charging and discharging is considered, again, both catalysts reveal a good cycling stability over the investigated timeframe of 26 h. The charging–discharging curves are shown in Figure 7c. During the first six cycles, the behavior is different for the two catalysts. Co0.10/PPy gives a fast increase in required overpotentials, whereas this increase is less sharp for Co0.24/PPy.

Stable cycling behavior was reached after ≈ 10 cycles for both cells. In this stabilized region, Co0.24/PPy shows a slightly lower charging overpotential, whereas Co0.10/PPy exhibits a slightly lower discharging overpotential. After 40 cycles, the round-trip overpotential ($E_{charge} - E_{discharge}$) is 0.94 V for Co0.10/PPy and 0.95 V for Co0.24/PPy, in comparison with 0.71 V and 0.69 V within the first cycle, respectively. This results in voltaic efficiencies ($E_{charge}/E_{discharge}$) of 56 % for Co0.10/PPy and 55 % for Co0.24/PPy.

In Table 2, the bifunctional Zn-air performance of Co0.10/PPy and Co0.24/PPy is compared with similar CoNC catalysts and a metal-free N-doped carbon catalyst, as well as a bifunctional noble metal catalyst commonly used for reference.

Co0.10/PPy and Co0.24/PPy show maximum power densities similar to Pt/C–RuO₂ catalyst, but less compared with other Co- or Fe/Co-based catalysts. It shows that despite the good OER/ORR performance, an optimization process is necessary to enhance the performance in a zinc-air cell. However, despite the rather high initial potential gaps of Co0.10/PPy and Co0.24/PPy, the increase in potential gap until the end of cycling is lower compared with Pt/C–RuO₂ and also lower compared with some other cobalt-based catalysts. Thus, we conclude that Co0.10/PPy and Co0.24/PPy exhibit decent cycling stability. After cycling, a second polarization curve was recorded for the catalysts (Figure 7b, curves ii), which is rarely done in the literature. Co0.10/PPy and Co0.24/PPy again show very similar performance after cycling. The power output decreased to $34.2\ mW\ cm^{-2}$ at $67.8\ mA\ cm^{-2}$ for Co0.10/PPy and $34.2\ mW\ cm^{-2}$ at $64.2\ mA\ cm^{-2}$ for Co0.24/PPy, which gives power losses of 44 and 45 %. After disassembling the cell, large bubbles were observed at the catalyst layer surface. Thus, the power losses might be assigned to a lowering of the accessible surface area by these bubbles rather than an intrinsic deactivation. Nonetheless, further work will be required to optimize the operation conditions.

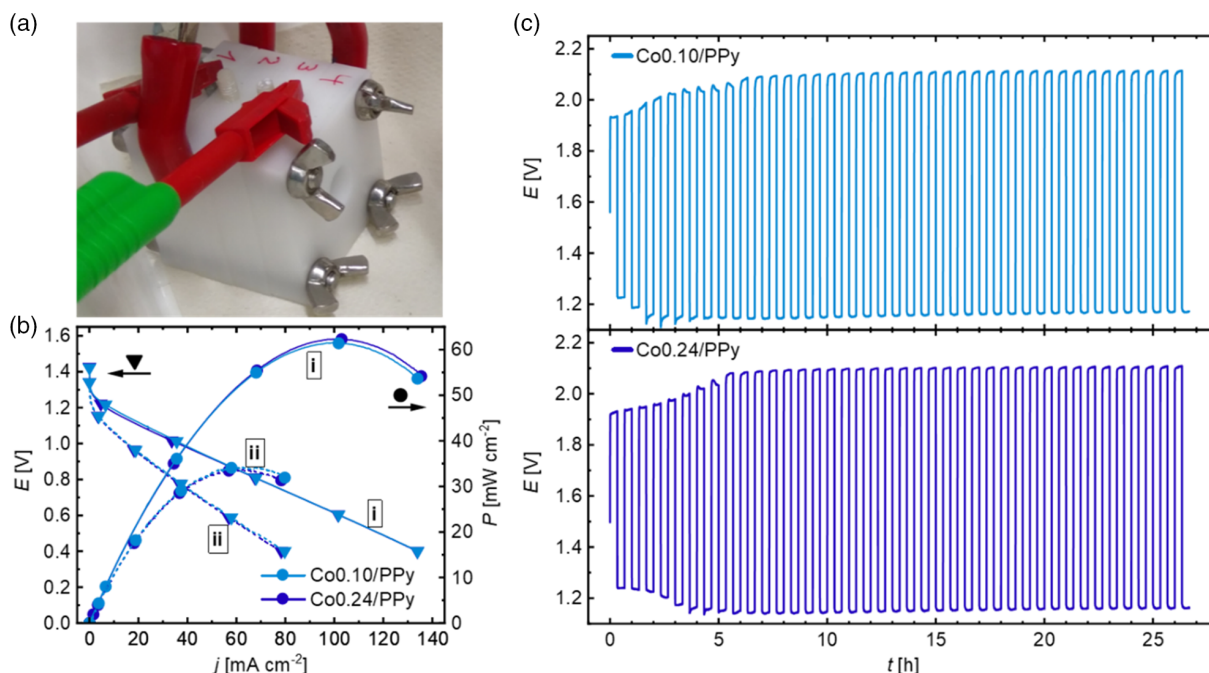


Figure 7. a) Photograph of the zinc-air cell, b) polarization curves and corresponding power density curves of Co_{0.10}/PPy and Co_{0.24}/PPy before (i) and after (ii) cycling, c) charge–discharge cycles with 2 mA cm⁻² of Co_{0.10}/PPy (blue line) and Co_{0.24}/PPy (purple line) with 40 min per each cycle. All measurements were performed in 6 M KOH with 0.2 M Zn acetate.

Table 2. Comparison of various bifunctional catalysts in Zn-air cells.

Sample	Description	Electrolyte	Catalyst loading [mg cm ⁻²]	P_{max} [mW cm ⁻²]	$j_{cycling}$ [mA cm ⁻²]	$\Delta E_{initial}$ [V]	n_{cycles}	ΔE after n_{cycles} [V]	Reference
Co _{0.10} /PPy	Co-impregnated PPy-NTs	6 M KOH + 0.2 M Zn(OAc) ₂	1	61.5	2	0.71	40	0.94	This work
Co _{0.24} /PPy	Co-impregnated PPy-NTs	6 M KOH + 0.2 M Zn(OAc) ₂	1	62.4	2	0.69	40	0.95	This work
Pt/C–RuO ₂	Bifunctional noble metal catalyst	6 M KOH + 0.2 M Zn(OAc) ₂	1	62	2	0.82	80	1.37	[17a]
CoNMC–700–1	Co _{5.47} N loaded N-doped carbon	6 M KOH + 0.2 M Zn(OAc) ₂	1	70	2	1.17	80	0.99	[17a]
NGM–Co	Co–N _x –C in hierarchical graphene mesh	6 M KOH + 0.2 M ZnCl ₂	0.5	150	2	≈1.00	60	≈1.15	[45]
FeCo–N–C–700	Fe, Co in MOF-derived N-doped carbon	6 M KOH + 0.2 M Zn(OAc) ₂	0.8	150	1	0.33	360	0.52	[47]
					5	0.46	240	0.66	
S-CoNC	Isolated Co–N sites on N-doped graphene	6 M KOH + 0.2 M ZnCl ₂	1	194	5	≈0.25	60	≈0.70	[51]
Co/Co ₃ O ₄ @PGS	Co/Co ₃ O ₄ in porous graphitized shells	6 M KOH + 0.2 M Zn(OAc) ₂	0.9	118	10	0.91	750	0.96	[52]
GNCNTs-4	Metal-free 2D N-doped CNT/graphene	6 M KOH + 0.2 M Zn(OAc) ₂	1	253	5	0.76	9000	0.85	[53]

3. Conclusion

In summary, various polypyrrole-based MNC catalysts were synthesized and electrochemically tested. Out of the investigated metals, the addition of cobalt led to the best-performing catalyst with an OER/ORR potential gap of 0.79 V, as well as a maximum power output of 62 mW cm⁻² in a zinc-air battery. The bifunctional behavior is attributed to an interaction of CoN₄ centers for the ORR and Co-oxide particles (transforming to hydroxides) for the OER. While this work displays great promise for the

fabricating of nonprecious metal-based bifunctional catalysts, further characterization as well as mechanistic studies are necessary to fully understand and optimize their electrochemical behavior and to improve the cell performance.

4. Experimental Section

Preparation of the Catalysts: The catalysts were prepared by a heat treatment of a precursor containing polypyrrole nanotubes and metal chlorides. The synthesis of polypyrrole nanotubes (PPy-NTs) was conducted

based on chemical oxidation of pyrrole with iron(III) chloride in the presence of methyl orange serving as structuring agent,^[41] the exact conditions can be found in Ni et al.^[34b] and is only summarized here, briefly. Pyrrole and methyl orange were dissolved in deionized water and a solution of iron(III) chloride (FeCl₃) was added dropwise under vigorous stirring. The mixture was left for polymerization at -10 °C for 16 h. After unfreezing, the nanotubes were filtered and washed ten times with an acetone/water mixture to remove iron chlorides and methyl orange residuals and dried. 0.20 mmol (0.05, 0.10, 0.24, and 0.40 mmol) of the transition metal chlorides were added to a slurry containing PPy-NTs (200 mg) in an ethanol/water mixture (3:1 v:v, 40 mL) and pestled for 10 min before evaporating the solvents and drying at 100 °C for 2 h.

For this variation series, the following metal precursors were used: CoCl₂ · 6H₂O, FeCl₃, MoCl₃, VCl₃, and WCl₆. As a second series, the cobalt content was varied (0.05, 0.10, 0.24, and 0.40 mmol), as Co turned out most promising.

The obtained impregnated precursors were then pyrolyzed in a microwave at a power of 600 W for 1 h in a quartz glass tube under constant flow of nitrogen to obtain the catalysts. The catalysts were directly used, without any further purification step. Thus, in addition to the expected MN₄ contribution, metal, nitride, or carbide species might have been formed during the preparation and either directly contribute to the catalytic activity or in a surface oxidized form. The sample label indicates the type of metal species and mole equivalent of the metal salt. For example, Co0.24/PPy is related to the catalyst prepared from 0.24 mmol cobalt chloride with 200 mg of PPy-NT.

For verification of our ORR and OER contribution assignments, the Co0.24/PPy catalyst was subjected to a subsequent acid leaching by dispersing in 1 M HCl under nitrogen atmosphere. The dispersion was sonicated for 2.5 h at 50 °C, left for 16 h under nitrogen atmosphere and was finally washed with 5 × 100 mL water.

Material Characterization: XRD was carried out in transmission mode on a StadiP diffractometer (Stoe & Cie. GmbH, Darmstadt) using Cu Kα1 radiation (Ge[111]-monochromator, λ = 1.5406 Å). Raman spectra were collected on a WiTec alpha300 R confocal Raman microscope with a laser excitation wavelength of 532 nm at a laser power of 2 mW. The spectra were recorded with 200 accumulations with an integration time of 0.75 s.

Electrochemical Characterization and Cell Test: Electrochemical measurements were carried out on a Princeton Applied Research Parstat 3000 A-DX bipotentiostat. The three-electrode configuration consisted of a RRDE as working electrode(s), a glassy carbon rod as counter electrode and a Hg/HgO reference electrode (3 M KOH).

Catalyst inks were prepared by mixing 5 mg catalyst powder with 142 μL deionized water, 25 μL Nafion solution (5 wt%) and 83.3 μL isopropanol, followed by 30 min treatment in an ultrasonic bath, 30 s with an ultrasonic rod and vortex-mixing for further 30 s. An ink volume of 6 μL was dropped onto the glassy carbon disc and dried in a weak compressed air flow for 2 min, resulting in a catalyst loading of 0.5 mg cm⁻².

The measurements were conducted at ambient temperature in 60 mL 0.1 M KOH electrolyte.

Prior to OER and ORR measurements, CVs in N₂ saturated electrolyte between 1.1 and 0.0 V were carried out at scan rates of 300 (20 cycles), 200, 100, 50, and 10 mV s⁻¹ (1 cycle each). OER performance was recorded in the same electrolyte within a potential range of 1.1 and 1.9 V (vs reversible hydrogen electrode, RHE) at a scan rate of 5 mV s⁻¹ at a rotation of 1500 rpm. ORR measurements were carried out on a fresh electrode in oxygen-saturated electrolyte at potentials between 1.1 and 0.0 V (vs RHE) at a scan rate of 10 mV s⁻¹ and rotation rates of 200, 400, 900, 1500, and 2500 rpm. The ORR curves of all rotation rates can be found in the Supporting Information. OER and ORR data were corrected for the electrolyte resistance between the electrodes by performing electrochemical impedance spectroscopy (EIS) prior to each measurement.

For the zinc-air cell tests, a 1 mg cm⁻² catalyst-loaded carbon paper gas diffusion layer GDL (Freudenberg GDL H23C9) served as air breathing cathode, a zinc plate (Alfa Aesar, 0.25 mm thickness, polished with 1 μm diamond particle polish) was used as anode and a separator membrane (Celgard 5550) was located between the electrodes. The same ink as

for the RRDE experiments was used. The ink was applied via drop-casting and dried on ambient air. The active area of the cathode was 0.79 cm⁻². The cell was operated with 6 M KOH + 0.2 M zinc acetate as electrolyte. Polarization curves were recorded by discharging the cell from OCV to 0.4 V at a sweep rate of 1 mV s⁻¹. For stability testing, the cells were charged and discharged 40 times with 2 mA cm⁻² for 40 min per cycle, leading to a protocol of ≈26 h. After cycling, a second polarization curve was recorded with the same conditions as previously mentioned.

Supporting Information

Supporting Information is available from the Wiley Online Library or from the author.

Acknowledgements

U.I.K. gratefully acknowledges financial support through the Adolf Messer award by the Dr Hans Messer Stiftung that enabled the microwave supply. U.I.K. and V.G. thank the BMBF for financial support through the young research group Fe-N-C StRedO (03XP0092).

Open access funding enabled and organized by Projekt DEAL.

Conflict of Interest

The authors declare no conflict of interest.

Data Availability Statement

The data that support the findings of this study are available from the corresponding authors upon reasonable request.

Keywords

bifunctional catalysts, metal-air batteries, nonprecious metal catalysts, oxygen reduction reaction, polypyrrole

Received: December 18, 2020

Revised: March 11, 2021

Published online: May 31, 2021

- [1] a) B. Dunn, H. Kamath, J.-M. Tarascon, *Science* **2011**, *334*, 928; b) N. Chawla, *Mater. Today Chem.* **2019**, *12*, 324; c) M. Catenacci, E. Verdolini, V. Bosetti, G. Fiorese, *Energy Policy* **2013**, *61*, 403.
- [2] R. van Noorden, *Nature* **2014**, *507*, 26.
- [3] a) O. Hass, F. Holzer, K. Müller, S. Müller, in *Handbook of Fuel Cells* (Ed: W. Vielstich), Wiley Interscience, New York **2010**; b) V. Caramia, B. Bozzini, *Mater. Renewable Sustainable Energy* **2014**, *3*, 2265; c) R. Cao, J.-S. Lee, M. Liu, J. Cho, *Adv. Energy Mater.* **2012**, *2*, 816.
- [4] a) Y. Li, J. Lu, *ACS Energy Lett.* **2017**, *2*, 1370; b) Y. Li, H. Dai, *Chem. Soc. Rev.* **2014**, *43*, 5257.
- [5] J. Fu, Z. P. Cano, M. G. Park, A. Yu, M. Fowler, Z. Chen, *Adv. Mater.* **2017**, *29*, 1604685.
- [6] X. Zhang, X.-G. Wang, Z. Xie, Z. Zhou, *Green Energy Environ.* **2016**, *1*, 4.
- [7] J. Masa, W. Xia, I. Sinev, A. Zhao, Z. Sun, S. Grützke, P. Weide, M. Muhler, W. Schuhmann, *Angew. Chem., Int. Ed.* **2014**, *53*, 8508.
- [8] Z. Chen, A. Yu, D. Higgins, H. Li, H. Wang, Z. Chen, *Nano Lett.* **2012**, *12*, 1946.
- [9] K. Zhang, L. Zhang, X. Chen, X. He, X. Wang, S. Dong, P. Han, C. Zhang, S. Wang, L. Gu, G. Cui, *J. Phys. Chem. C* **2013**, *117*, 858.

- [10] Y. Qian, Z. Hu, X. Ge, S. Yang, Y. Peng, Z. Kang, Z. Liu, J. Y. Lee, D. Zhao, *Carbon* **2017**, *111*, 641.
- [11] a) S. Fu, C. Zhu, J. Song, D. Du, Y. Lin, *Adv. Energy Mater.* **2017**, *7*, 1700363; b) J. Stacy, Y. N. Regmi, B. Leonard, M. Fan, *Renewable Sustainable Energy Rev* **2017**, *69*, 401; c) K. N. Wood, R. O'Hayre, S. Pylypenko, *Energy Environ. Sci.* **2014**, *7*, 1212.
- [12] a) L. Osmieri, A. H. Monteverde Videla, S. Specchia, *Int. J. Hydrogen Energy* **2016**, *41*, 19610; b) N. R. Sahraie, U. I. Kramm, J. Steinberg, Y. Zhang, A. Thomas, T. Reier, J.-P. Paraknowitsch, P. Strasser, *Nat. Commun.* **2015**, *6*, 8618.
- [13] U. I. Kramm, I. Herrmann-Geppert, J. Behrends, K. Lips, S. Fiechter, P. Bogdanoff, *J. Am. Chem. Soc.* **2016**, *138*, 635.
- [14] a) U. I. Kramm, J. Herranz, N. Larouche, T. M. Arruda, M. Lefèvre, F. Jaouen, P. Bogdanoff, S. Fiechter, I. Abs-Wurmbach, S. Mukerjee, J.-P. Dodelet, *Phys. Chem. Chem. Phys.* **2012**, *14*, 11673; b) U. I. Kramm, M. Lefèvre, N. Larouche, D. Schmeisser, J.-P. Dodelet, *J. Am. Chem. Soc.* **2014**, *136*, 978; c) A. Zitolo, V. Goellner, V. Armel, M.-T. Sougrati, T. Mineva, L. Stievano, E. Fonda, F. Jaouen, *Nat. Mater.* **2015**, *14*, 937.
- [15] a) J. Zhang, D. He, H. Su, X. Chen, M. Pan, S. Mu, *J. Mater. Chem. A* **2014**, *2*, 1242; b) U. I. Kramm, I. Herrmann-Geppert, P. Bogdanoff, S. Fiechter, *J. Phys. Chem. C* **2011**, *115*, 23417; c) M. T. Sougrati, V. Goellner, A. K. Schuppert, L. Stievano, F. Jaouen, *Catal. Today* **2016**, *262*, 110.
- [16] a) X. Liu, I. S. Amiinu, S. Liu, K. Cheng, S. Mu, *Nanoscale* **2016**, *8*, 13311; b) Y. Liu, H. Jiang, Y. Zhu, X. Yang, C. Li, *J. Mater. Chem. A* **2016**, *4*, 1694; c) G. Wu, A. Santandreu, W. Kellogg, S. Gupta, O. Ogoke, H. Zhang, H.-L. Wang, L. Dai, *Nano Energy* **2016**, *29*, 83.
- [17] a) Z. Rong, C. Dong, S. Zhang, W. Dong, F. Huang, *Nanoscale* **2020**, *12*, 6089; b) L. Wang, W. Zhang, X. Zheng, Y. Chen, W. Wu, J. Qiu, X. Zhao, X. Zhao, Y. Dai, J. Zeng, *Nat. Energy* **2017**, *2*, 869.
- [18] C. M. Ghimbeu, E. Raymundo-Piñero, P. Fioux, F. Béguin, C. Vix-Guterl, *J. Mater. Chem.* **2011**, *21*, 13268.
- [19] A. Pawbake, R. Waykar, A. Jadhavar, R. Kulkarni, V. Waman, A. Date, D. Late, H. Pathan, S. Jadhkar, *Mater. Lett.* **2016**, *183*, 315.
- [20] a) S.-X. Guo, Y. Liu, A. M. Bond, J. Zhang, P. Esakki Karthik, I. Maheshwaran, S. Senthil Kumar, K. L. N. Phani, *Phys. Chem. Chem. Phys.* **2014**, *16*, 19035; b) C.-W. Tang, C.-B. Wang, S.-H. Chien, *Thermochim. Acta* **2008**, *473*, 68.
- [21] Y.-S. Li, J. S. Church, A. L. Woodhead, *J. Magn. Magn. Mater.* **2012**, *324*, 1543.
- [22] F. Ureña-Begara, A. Crunteanu, J.-P. Raskin, *Appl. Surf. Sci.* **2017**, *403*, 717.
- [23] a) A. Amulevičius, D. Baltrūnas, A. Daugvila, R. Davidonis, K. Mažeika, V. Remeikis, Č. Sipavičius, A. Undzėnas, *Lithuanian J. Phys.* **2009**, *49*, 221; b) V. A. Svetlichnyi, A. V. Shabalina, I. N. Lapin, D. A. Goncharova, D. A. Velikanov, A. E. Sokolov, *Appl. Surf. Sci.* **2018**, *462*, 226; c) M. Bauer, P. Davydovskaya, M. Janko, M. Kaliwoda, N. Petersen, S. Gilder, R. W. Stark, *J. Raman Spectrosc.* **2011**, *42*, 1413.
- [24] F. Tuinstra, J. L. Koenig, *J. Chem. Phys.* **1970**, *53*, 1126.
- [25] A. Zana, J. Speder, N. E. Reeler, T. Vosch, M. Arenz, *Electrochim. Acta* **2013**, *114*, 455.
- [26] A. Oya, S. Ōtani, *Carbon* **1979**, *17*, 131.
- [27] a) A. M. Schwenke, S. Hoepfener, U. S. Schubert, *Adv. Mater.* **2015**, *27*, 4113; b) M. Gupta, W. L. Wong, *Microwaves and Metals*, John Wiley & Sons, New York **2007**; c) K. Kinoshita, *Carbon. Electrochemical and Physicochemical Properties*, 1st ed., Wiley & Sons Ltd, New York **1988**.
- [28] a) E. O. Pentsak, V. A. Cherepanova, M. A. Sinayskiy, A. V. Samokhin, V. P. Ananikov, *Nanomaterials (Basel, Switzerland)* **2019**, *9*, 19; b) E. O. Pentsak, E. G. Gordeev, V. P. Ananikov, *ACS Catal.* **2014**, *4*, 3806.
- [29] A. M. Schwenke, S. Hoepfener, U. S. Schubert, *Adv. Mater.* **2015**, *27*, 4113.
- [30] a) E. Castro, C. Gervasi, J. Vilche, *J. Appl. Electrochem.* **1998**, *28*, 835; b) M. E. Lyons, M. P. Brandon, *J. Electroanal. Chem.* **2010**, *641*, 119; c) J. Li, S. Gadipelli, *Chemistry* **2020**, *26*, 14167.
- [31] B. S. Yeo, A. T. Bell, *J. Am. Chem. Soc.* **2011**, *133*, 5587.
- [32] a) Y. Zhao, B. Sun, X. Huang, H. Liu, D. Su, K. Sun, G. Wang, *J. Mater. Chem. A* **2015**, *3*, 5402; b) X. Lu, C. Zhao, *J. Mater. Chem. A* **2013**, *1*, 12053; c) X. Lu, H. M. Chan, C.-L. Sun, C.-M. Tseng, C. Zhao, *J. Mater. Chem. A* **2015**, *3*, 13371.
- [33] X. Chen, Z. Zhou, H. E. Karahan, Q. Shao, L. Wei, Y. Chen, *Small* **2018**, *14*, e1801929.
- [34] a) M. Kübler, S. Wagner, T. Jurzinsky, S. Paul, N. Weidler, E. D. Gomez Villa, C. Cremers, U. I. Kramm, *Energy Technol.* **2020**, *8*, 2000433; b) L. Ni, C. Gallenkamp, S. Paul, M. Kübler, P. Theis, S. Chhabra, K. Hofmann, E. Bill, A. Schnegg, B. Albert, V. Krewald, U. I. Kramm, *Adv. Energy Sustainability Res.* **2021**, *2*, 2000064.
- [35] T. S. Olson, S. Pylypenko, P. Atanassov, K. Asazawa, K. Yamada, H. Tanaka, *J. Phys. Chem. C* **2010**, *114*, 5049.
- [36] U. I. Kramm, R. Marschall, M. Rose, *ChemCatChem* **2019**, *11*, 2563.
- [37] S. Jung, C. C. L. McCrory, I. M. Ferrer, J. C. Peters, T. F. Jaramillo, *J. Mater. Chem. A* **2016**, *4*, 3068.
- [38] a) F. Jaouen, J.-P. Dodelet, *Electrochim. Acta* **2007**, *52*, 5975; b) G. Wu, C. M. Johnston, N. H. Mack, K. Artyushkova, M. Ferrandon, M. Nelson, J. S. Lezama-Pacheco, S. D. Conradson, K. L. More, D. J. Myers, P. Zelenay, *J. Mater. Chem.* **2011**, *21*, 11392.
- [39] A. Shahraei, M. Kuebler, I. Martinaioui, K. A. Creutz, W. D. Z. Wallace, M. A. Nowroozi, S. Paul, N. Weidler, R. W. Stark, O. Clemens, U. I. Kramm, *J. Mater. Chem. A* **2018**, *6*, 22310.
- [40] M. Ferrandon, A. J. Kropf, D. J. Myers, K. Artyushkova, U. Kramm, P. Bogdanoff, G. Wu, C. M. Johnston, P. Zelenay, *J. Phys. Chem. C* **2012**, *116*, 16001.
- [41] a) J. Kopecký, D. Kopecký, M. Vršata, P. Fitl, J. Stejskal, M. Trchová, P. Bober, Z. Morávková, J. Prokeš, I. Sapurina, *RSC Adv.* **2014**, *4*, 1551; b) Y. Li, P. Bober, M. Trchová, J. Stejskal, *J. Mater. Chem. C* **2017**, *5*, 4236.
- [42] M. Zhang, Q. Dai, H. Zheng, M. Chen, L. Dai, *Adv. Mater.* **2018**, *30*, 1705431.
- [43] G. Jia, W. Zhang, G. Fan, Z. Li, D. Fu, W. Hao, C. Yuan, Z. Zou, *Angew. Chem., Int. Ed.* **2017**, *56*, 13781.
- [44] L. Ma, S. Chen, Z. Pei, Y. Huang, G. Liang, F. Mo, Q. Yang, J. Su, Y. Gao, J. A. Zapien, C. Zhi, *ACS Nano* **2018**, *12*, 1949.
- [45] C. Tang, B. Wang, H.-F. Wang, Q. Zhang, *Adv. Mater.* **2017**, *29*, 1703185.
- [46] I. S. Amiinu, X. Liu, Z. Pu, W. Li, Q. Li, J. Zhang, H. Tang, H. Zhang, S. Mu, *Adv. Funct. Mater.* **2018**, *28*, 1704638.
- [47] X. Duan, S. Ren, N. Pan, M. Zhang, H. Zheng, *J. Mater. Chem. A* **2020**, *8*, 9355.
- [48] Y. Chen, S. Hu, F. Nichols, F. Bridges, S. Kan, T. He, Y. Zhang, S. Chen, *J. Mater. Chem. A* **2020**, *8*, 11649.
- [49] C.-Y. Su, H. Cheng, W. Li, Z.-Q. Liu, N. Li, Z. Hou, F.-Q. Bai, H.-X. Zhang, T.-Y. Ma, *Adv. Energy Mater.* **2017**, *7*, 1602420.
- [50] T. Sun, J. Wang, C. Qiu, X. Ling, B. Tian, W. Chen, C. Su, *Adv. Sci.* **2018**, *5*, 1800036.
- [51] J. Wu, H. Zhou, Q. Li, M. Chen, J. Wan, N. Zhang, L. Xiong, S. Li, B. Y. Xia, G. Feng, M. Liu, L. Huang, *Adv. Energy Mater.* **2019**, *9*, 1900149.
- [52] Y. Jiang, Y.-P. Deng, J. Fu, D. U. Lee, R. Liang, Z. P. Cano, Y. Liu, Z. Bai, S. Hwang, L. Yang, D. Su, W. Chu, Z. Chen, *Adv. Energy Mater.* **2018**, *8*, 1702900.
- [53] Y. Xu, P. Deng, G. Chen, J. Chen, Y. Yan, K. Qi, H. Liu, B. Y. Xia, *Adv. Funct. Mater.* **2020**, *30*, 1906081.